Communications of BAO, Vol. 73, Issue 2, 2026, pp. 273-280

From global estimates to longitudinal asymmetries: a multi-tracer view of the Galactic Star Formation Rate

D. Elia *[1] and N. J. Evans[2]

[1]INAF-Istituto di Astrofisica e Planetologia Spaziale, Roma, Italy
[2]Department of Astronomy, The University of Texas at Austin, Austin, Texas, USA

Abstract

The Star Formation Rate (SFR) of the Milky Way can be measured from Hi-GAL far-infrared photometric data in two ways: from the masses of compact sources (clumps), or from the extended 70 μm emission assigned the distance of the nearest dense clump. It can also be derived independently from the physical properties of CO molecular clouds. The total SFR and its radial distribution based on these three different methods show remarkable agreement, and the total SFR ($\sim 1.4-1.7\,M_\odot\,yr^{-1}$) agrees with independent measurements. This result allows consideration of non-axisymmetric structures, using a plot of the longitude dependence of the SFR. An East-West (fourth quadrant versus first quadrant) asymmetry clearly appears, with an excess for $\ell \leq 40°$ and negative dips at $40° \leq \ell \leq 74°$, ruling out a purely circular axisymmetric distribution.

Keywords: *Milky Way Galaxy; Star formation; Far infrared astronomy; Interstellar medium.*

1. Introduction

The Star Formation Rate (SFR) is one of the most fundamental macroscopic properties governing the structural evolution, gas consumption dynamics, and chemical enrichment of galaxies across cosmic time. In extragalactic astronomy, global SFRs are routinely derived using spatially integrated, monochromatic or hybrid flux indicators spanning various wavelength regimes (e.g., Kennicutt, 1998):

- Hα line emission: directly tracing recombination radiation from photoionized H II regions around massive stars ($M \gtrsim 10\,M_\odot$) on short timescales ($\sim 3-10$ Myr) (e.g., Calzetti et al., 2007, Kennicutt, 1998);
- Far-Ultraviolet (FUV) continuum: measuring photospheric emission from non-ionizing O- and B-type stars on longer timescales ($\sim 10-100$ Myr), though heavily affected by dust attenuation (e.g., Kennicutt & Evans, 2012, Salim et al., 2007);
- Mid-to-Far-Infrared (MIR/FIR) continuum (e.g., 24 μm, 70 μm): measuring stellar UV/visible radiation re-processed and thermalized by interstellar dust grains over timescales of $\sim 10-100$ Myr (e.g., Calzetti et al., 2010, Li et al., 2010);
- Radio free-free continuum: tracing optically thin thermal bremsstrahlung emission from ionized gas again on short timescales ($\sim 3-10$ Myr), free from dust extinction biases (e.g., Murphy et al., 2011).

However, these extragalactic relations are inherently calibrated on populations of massive stars and are thus subject to notable systematic uncertainties, including sensitivity to the adopted Initial Mass Function (IMF) sampling, extinction corrections, and time-scale assumptions for stellar feedback.

In this context, the Milky Way provides a unique, high-resolution laboratory where star-forming regions can be dissected down to the scale of individual molecular clouds ($10-100$ pc) and dense, star-forming clumps ($0.3-3$ pc). Unlike distant galaxies, where sub-kpc structural details are blended into single beam footprints, Galactic observations allow us to directly count young stellar objects (e.g., Robitaille & Whitney,

*davide.elia@inaf.it, Corresponding author

2010), measure gamma-ray/decay signatures such as ^{26}Al nucleosynthesis (e.g., Diehl et al., 2006), evaluate radio free-free ionization rates (e.g., Murray & Rahman, 2010), measure gas densities across different phase transitions, and map star formation activity with localized spatial information.

Despite these advantages, establishing a reliable global SFR for the Galaxy has historically been challenging due to "inside-out" observational perspectives: lines-of-sight severe extinction, kinematic distance ambiguities in the Galactic disk, and incomplete latitude coverage off the midplane. Over the past decades, independent estimates have spanned a range from $< 1\,\mathrm{M}_\odot\,\mathrm{yr}^{-1}$ to $> 3\,\mathrm{M}_\odot\,\mathrm{yr}^{-1}$, eventually converging toward an accepted reference value of $1.65 \pm 0.19\,\mathrm{M}_\odot\,\mathrm{yr}^{-1}$ (Chomiuk & Povich, 2011, Licquia & Newman, 2015).

A major leap forward in unifying our global and local understanding of Galactic star formation was achieved by the Herschel InfraRed Galactic Plane Survey (Hi-GAL, Molinari et al., 2010). By mapping the whole Galactic plane with a 2°-wide latitude strip in five FIR continuum bands between 70 μm and 500 μm, Hi-GAL yielded unprecedented catalogs of hundreds of thousands of compact cold dust sources across all evolutionary stages—from starless and prestellar clumps to protostellar embedded systems(Elia et al., 2017, 2021, Molinari et al., 2016). In two recent papers, Elia et al. (2022) and Elia et al. (2025) systematically exploited the vast Hi-GAL data product tree to reconstruct both the 1D Galactocentric profile and 2D face-on distribution of the Galactic SFR:

1) Elia et al. (2022) established a bottom-up, clump-mass-based formulation applied to over 30,000 star forming clumps provided with distance estimates. By tracing the evolution of dense clumps in the luminosity-mass diagram, they yielded a global SFR lower limit of $1.7 \pm 0.6\,\mathrm{M}_\odot\,\mathrm{yr}^{-1}$, which increases to $2.0 \pm 0.7\,\mathrm{M}_\odot\,\mathrm{yr}^{-1}$ when accounting for sources lacking distance determinations via Monte Carlo spatial sampling.

2) Elia et al. (2025) refined this picture along three critical axes: (*i*) incorporating a realistic radial variation in the gas-to-dust ratio (γ) driven by abundance gradients across the Galactic disk; (*ii*) testing the extragalactic monochromatic 70 μm SFR tracer directly on the diffuse and extended emission maps of the Milky Way; and (*iii*) comparing observational SFR distributions against theoretical star formation efficiency models applied to CO molecular cloud catalogs (e.g., Evans et al., 2022).

In this paper, we review the main findings of these studies and exploit their datasets to evaluate the longitudinal distribution of the Galactic SFR, comparing the clump-mass and extended 70 μm tracers across the disk. We introduce an East–West asymmetry parameter, $B(\ell)$, and compare it with the prediction of a purely circular, axisymmetric disk.

2. Recent multi-approach estimates of the Galactic SFR

2.1. Global and radial SFR from Hi-GAL clumps

The contribution $\mathrm{SFR_{mc}}$ given by an individual clump to the SFR is computed by Elia et al. (2022) via evolutionary models in the luminosity-mass diagram, parameterized as:

$$\left(\frac{\mathrm{SFR_{mc}}}{\mathrm{M}_\odot\ \mathrm{yr}^{-1}}\right) = 5.6 \times 10^{-7} \left(\frac{M_{\mathrm{cat}}}{\mathrm{M}_\odot}\right)^{0.74} \tag{1}$$

In that paper, clump masses were derived assuming a constant solar-neighborhood gas-to-dust ratio $\gamma = 100$. However, elemental abundance gradients across the disk (e.g., Giannetti et al., 2017, Muñoz-Mateos et al., 2009) imply that γ increases with Galactocentric distance (R_{Gal}). Elia et al. (2025) introduced a corrected radial profile for $\gamma(R_{\mathrm{Gal}})$ based on the physical requirement that the median surface density of prestellar clumps remains constant across the Galaxy:

$$\log[\gamma(R_{\mathrm{Gal}})] = (0.051 \pm 0.001)\left(\frac{R_{\mathrm{Gal}} - R_0}{\mathrm{kpc}}\right) + 2 \tag{2}$$

Applying this correction adjusts the global clump-based SFR estimate from $1.96 \pm 0.73\,\mathrm{M}_\odot\,\mathrm{yr}^{-1}$ (Elia et al., 2022) down to $1.65 \pm 0.61\,\mathrm{M}_\odot\,\mathrm{yr}^{-1}$ (Elia et al., 2025), bringing it into exact agreement with independent multi-method literature estimates ($1.65 \pm 0.19\,\mathrm{M}_\odot\,\mathrm{yr}^{-1}$, Licquia & Newman, 2015).

2.2. Extragalactic calibration: the 70 μm monochromatic indicator

Extragalactic studies often employ monochromatic 70 μm luminosity as a proxy for SFR (e.g., Li et al., 2010). Applying this relation directly to individual Hi-GAL catalog source fluxes fails by two orders of magnitude (SFR $\sim 0.024\,M_\odot\,\mathrm{yr}^{-1}$). As demonstrated in Elia et al. (2025), this failure occurs because $\sim 96-98\%$ of the 70 μm flux resides in extended, diffuse emission surrounding the compact clumps. By re-projecting the survey into 72 mosaics, each covering a 5° interval in longitude, and assigning distances to diffuse pixels based on the nearest catalog source in terms of angular separation, Elia et al. (2025) found $\mathrm{SFR}_{70} = 1.42^{+0.63}_{-0.44}\,M_\odot\,\mathrm{yr}^{-1}$ from the total extended 70 μm emission.

2.3. Star Formation Rate from CO cloud catalogs (the EKO model)

Beyond dust-based Herschel estimators, Elia et al. (2025) integrated a third independent method based on the theoretical framework of Kim et al. (2021) and Evans et al. (2022, hereafter EKO) applied to the ^{12}CO(1 → 0) cloud catalog of Miville-Deschênes et al. (2017). To homogenize these data with Hi-GAL, cloud distances were recomputed using the Russeil et al. (2017) rotation curve. Cloud masses and sizes were rescaled accordingly, adjusting the luminosity-to-mass conversion factor α_{CO} across the Galactic disk to account for the radial metallicity gradient:

$$\alpha_{\mathrm{CO}} = 4.50\,Z^{-0.80} \quad \left[M_\odot\,(\mathrm{K\,km\,s^{-1}\,pc^2})^{-1}\right] \tag{3}$$

with the metallicity, relative to the solar circle set to $Z_\odot = 1$, decreasing as $\log Z = -0.044(R_{\mathrm{Gal}}/\mathrm{kpc} - 8.34)$.

From the free-fall time t_{ff} and virial parameter α_{vir}, the efficiency per free-fall time was derived via $\epsilon_{\mathrm{ff}} = 0.30\exp(-2.018\,\alpha_{\mathrm{vir}}^{1/2})$, yielding $\mathrm{SFR} = \epsilon_{\mathrm{ff}} M/t_{\mathrm{ff}}$ in individual clouds. This method predicts a total Galactic star formation rate of $\mathrm{SFR}_{\mathrm{EKO}} = 1.47\,M_\odot\,\mathrm{yr}^{-1}$, in striking agreement with clump-based ($1.46-1.65\,M_\odot\,\mathrm{yr}^{-1}$) and diffuse 70 μm ($1.42^{+0.63}_{-0.44}\,M_\odot\,\mathrm{yr}^{-1}$) values, as well as the aforementioned Licquia & Newman (2015) benchmark. Furthermore, the resulting radial profile $\Sigma_{\mathrm{SFR}}(R_{\mathrm{Gal}})$ matches the 70 μm distribution remarkably well out to ~ 20 kpc. Discrepancies appear only on localized 0.5 kpc face-on scales, showing that agreement emerges through galactic-scale statistical averaging.

3. Longitudinal distribution of the Galactic Star Formation Rate

While the Galactocentric radial profile $\Sigma_{\mathrm{SFR}}(R_{\mathrm{Gal}})$ has been extensively characterized in previous works (Elia et al., 2022, 2025), projecting the star formation rate directly along Galactic longitude provides fundamental insight into the distribution of star-forming activity as directly viewed from our internal vantage point. In Elia et al. (2022), the longitudinal profile was derived solely from the clump-mass method (their Figure 4), but with no mass correction, whereas in Elia et al. (2025) the comparison between the clump-mass and the 70 μm map-based approaches was discussed only in terms of regional ratios across 5° mosaics (their Figure 3).

In Figure 1, we present for the first time a direct, side-by-side comparison of the absolute SFR integrated in 2° bins of Galactic longitude across the entire disk for both techniques: the clump-mass method corrected for a radially variable gas-to-dust ratio (orange curve) and the extended 70 μm map integration (blue curve).

Both distributions exhibit striking morphological agreement on large scales: over 90% of the Galactic star formation is strictly confined within the inner longitudes ($|l| \leq 60°$), dropping precipitously towards the outer longitudes ($|l| > 90°$).

The prominent spikes associated with the most active starburst complexes — such as the Central Molecular Zone ($l \sim 0°$), W43 ($l \sim 30°$), W51 ($l \sim 49°$), and G337.3 ($l \sim 338°$) — are independently recovered at identical longitudes by both tracers.

Noticeable differences emerge on localized scales, reflecting the distinct physical nature of the two methods (extended emission vs. clump granularity): the 70 μm profile presents a smoother, continuous baseline because it includes the diffuse interstellar dust heated by both embedded clusters and the ambient radiation field. In contrast, the clump-based curve exhibits sharper, discrete peaks and deeper inter-complex dips, directly mirroring the Poissonian census of cataloged compact sources.

At the Galactic Center, the 70 μm emission produces a substantially higher peak ($\approx 0.13\,M_\odot\,\mathrm{yr}^{-1}$) compared to the clump-mass estimate ($\approx 0.04\,M_\odot\,\mathrm{yr}^{-1}$). This discrepancy is consistent with findings in Elia et al. (2025), where the dense clump catalog within $R_{\mathrm{Gal}} < 0.5$ kpc recovers less compact mass than

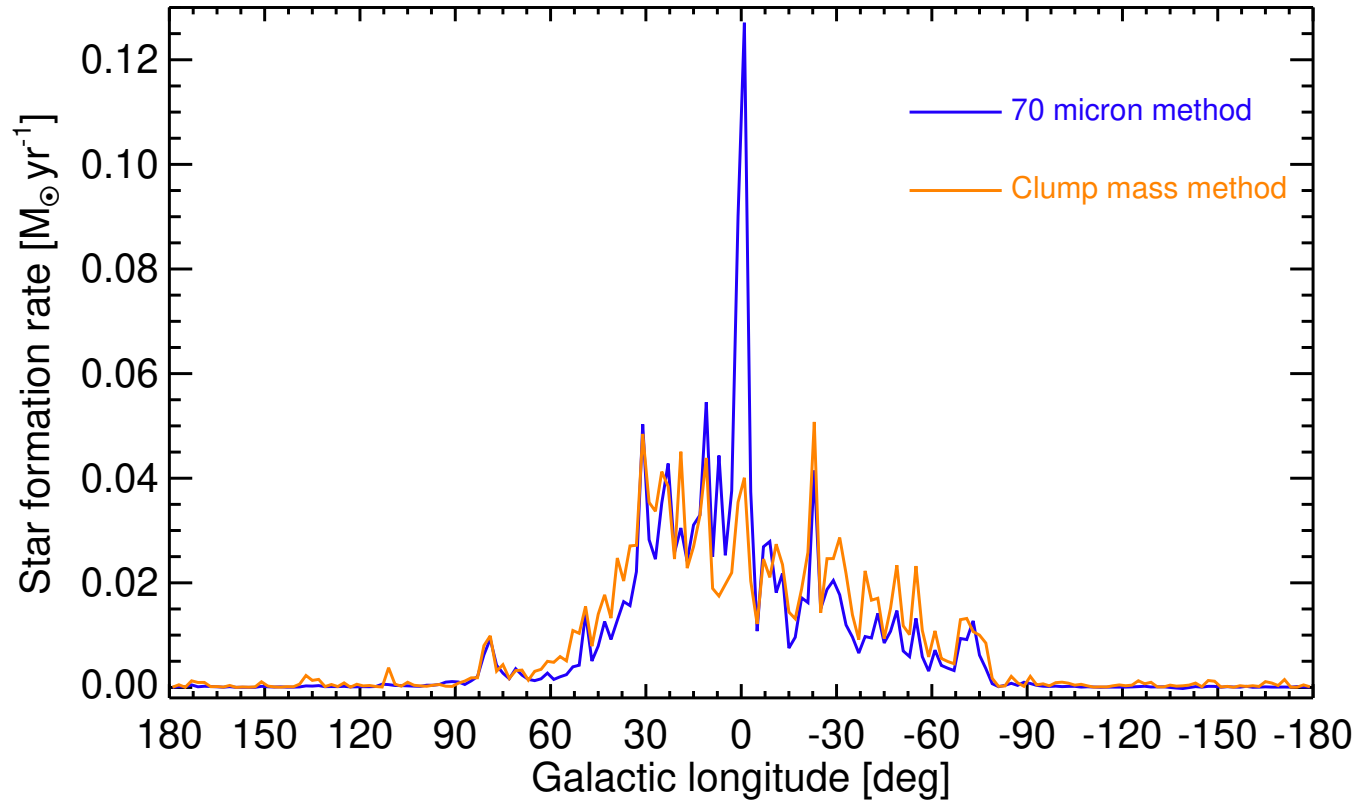

Figure 1. Distribution of the Milky Way star formation rate as a function of Galactic longitude, integrated in 2° bins over the range $-180° \leq l \leq +180°$. The orange curve represents the SFR derived from the Hi-GAL clump-mass method ($\mathrm{SFR_{mc}}$) corrected for the radial gradient of the gas-to-dust ratio. The blue curve shows the SFR obtained from the whole (compact plus extended) Hi-GAL 70 μm emission ($\mathrm{SFR_{70}}$) by assigning heliocentric distances to diffuse map pixels.

implied by diffuse FIR or extended molecular tracers, while diffuse 70 μm emission captures substantial photon reprocessing from the dense nuclear stellar cluster.

4. Quantifying longitudinal asymmetries

To quantify the degree of symmetry breaking of SFR across the Galactic disk as seen from the Sun, we compute the empirical longitudinal asymmetry parameter $B(\ell)$, comparing symmetric lines of sight between the first and fourth quadrants (Q1 and Q4, respectively):

$$B(\ell) = \frac{\mathrm{SFR}(\ell) - \mathrm{SFR}(360° - \ell)}{\mathrm{SFR}(\ell) + \mathrm{SFR}(360° - \ell)}, \qquad 0° \leq \ell \leq 90° \tag{4}$$

(cf. Blitz & Spergel, 1991).

In Figure 2, we show $B(\ell)$ evaluated in 2° longitude bins for both the 70 μm map integration (blue curve) and the clump-mass model (orange curve). The two tracers yield a strikingly consistent broad-scale pattern across the inner disk, and both highlight some relevant features:

- Inner disk asymmetry ($0° < \ell \lesssim 40°$): the B parameter is predominantly positive, with values consistently confined within the range $0.2 \lesssim B \lesssim 0.6$. This systematic excess in the Q1 traces the non-axisymmetric gas compression driven by the near end of the Galactic bar oriented toward positive longitudes, together with massive molecular complexes in the Molecular Ring such as W43 ($\ell \approx 31°$) and W49 ($\ell \approx 43°$).

- Spiral arm inversion ($40° \lesssim \ell \lesssim 74°$): the B parameter systematically drops to negative values (settling in the negative regime $-0.8 \lesssim B \lesssim -0.4$). In this range, line-of-sight geometries through the Q4 intersect prominent tangential sections of the Crux-Scutum and Centaurus arms, while corresponding lines of sight in the Q1 probe inter-arm regions.

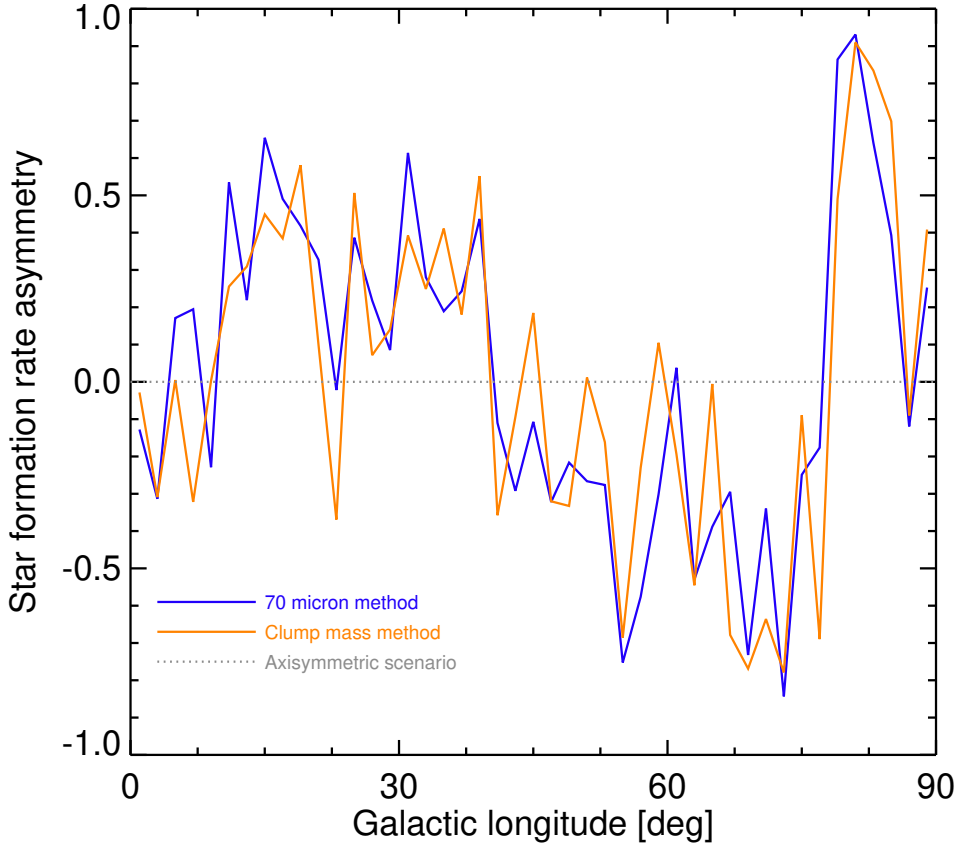

Figure 2. Longitudinal SFR asymmetry parameter, $B(\ell) = [\mathrm{SFR}(\ell) - \mathrm{SFR}(360^\circ - \ell)] \,/\, [\mathrm{SFR}(\ell) + \mathrm{SFR}(360^\circ - \ell)]$, computed in 2° bins of Galactic longitude across the Q1 and Q4. The blue curve represents the asymmetry derived from the whole Hi-GAL 70 μm emission maps, while the orange curve is obtained from the clump-mass method corrected for the radial gas-to-dust gradient (Elia et al., 2025). The theoretical prediction for a purely axisymmetric disk is overplotted as a grey dotted horizontal line at $B = 0$ (Appendix A).

- The Cygnus X starburst excursion ($74^\circ \lesssim \ell \lesssim 86^\circ$): both methods independently exhibit a dramatic surge approaching $B = 1$. This sharp feature is caused by the Cygnus X complex ($\ell \sim 78^\circ - 82^\circ$), one of the richest and most active massive star forming regions in the local/intermediate disk, which lacks any counterpart of comparable star forming activity at the symmetric southern longitude ($\ell \approx 280^\circ$).

5. Discussion

In classical spiral structure theory, grand-design spirals (e.g., M51) exhibit large-scale symmetry driven by a global density wave, whereas flocculent galaxies (e.g., NGC 2841) are characterized by stochastic, self-propagating star formation devoid of coherent large-scale patterns.

If the Milky Way were a pure grand-design spiral with axial symmetry, B would stay close to zero with only mild, low-frequency fluctuations. Similarly, a purely flocculent disk would generate uncorrelated, high-frequency noise around zero. Indeed, any purely circular, axisymmetric disk would show $B \equiv 0$, as demonstrated in Appendix A. This baseline is shown in Figure 2 as a horizontal dotted line at $B = 0$ and represents the idealized null hypothesis: any non-zero value directly measures non-axisymmetric structural perturbations (the Galactic bar, spiral arms, and localized molecular complexes).

The observed behavior of B, however, suggests a hybrid morphology for the Milky Way: the broad-scale coherence (i.e., the persistent positive plateau at $\ell < 40^\circ$ shifting smoothly to negative values at $40^\circ < \ell < 74^\circ$) reflects the global gravitational potential, shaped primarily by the non-axisymmetric potential of the central bar and prominent spiral arm tangencies. The superimposed sharp excursions (such as the Cygnus X peak at $\ell \approx 80^\circ$ and local dips) quantify the stochastic, flocculent contribution of individual giant molecular complexes and localized starbursts.

6. Conclusions

In this work, we presented an overview of recent determinations of the Galactic SFR and investigated the longitudinal distribution of star formation across the Milky Way disk by directly comparing the Hi-GAL clump-mass method with extended 70 μm emission. Our main conclusions are summarized as follows:

1) The longitudinal profiles of both the clump-based SFR (corrected for the radial gas-to-dust abundance gradient) and the diffuse 70 μm map integration show excellent overall morphological agreement, with more than 90% of Galactic star formation tightly confined within $|\ell| \leq 60°$.

2) By defining the longitudinal asymmetry parameter $B(\ell)$, we evaluated the symmetry of star formation across the Q1 and Q4. While any purely circular, axisymmetric disk yields $B(\ell) \equiv 0$ identically across all longitudes, the observed Milky Way exhibits coherent and pronounced deviations from this null hypothesis.

3) The observed asymmetry profile reveals a distinct two-component behavior: a broad-scale coherent pattern — characterized by a positive plateau ($B \sim +0.2$ to $+0.6$) at $\ell \leq 40°$ and a negative dip at intermediate longitudes — tracing the global non-axisymmetric potential of the Galaxy, alongside localized excursions (such as the prominent Cygnus X surge near $\ell \approx 80°$) driven by stochastic starburst events.

The asymmetry index $B(\ell)$ thus represents a straightforward diagnostic to quantify the relative roles of large-scale structural perturbations and localized star-forming complexes in the Galactic disk.

Acknowledgements

D.E. acknowledges financial support from the project SFR4ALL, funded by INAF (1.05.93.04) through the PRORIS call. N.J.E. is grateful to the Astronomy Department of the University of Texas for research support

References

Blitz L., Spergel D. N., 1991, Astrophys. J. , 379, 631

Calzetti D., et al., 2007, Astrophys. J. , 666, 870

Calzetti D., et al., 2010, Astrophys. J. , 714, 1256

Chomiuk L., Povich M. S., 2011, Astron. J. , 142, 197

Diehl R., et al., 2006, Nature. , 439, 45

Elia D., et al., 2017, Mon. Not. R. Astron. Soc. , 471, 100

Elia D., et al., 2021, Mon. Not. R. Astron. Soc. , 504, 2742

Elia D., et al., 2022, Astrophys. J. , 941, 162

Elia D., Evans II N. J., Soler J. D., Strafella F., Schisano E., Molinari S., Giannetti A., Patra S., 2025, Astrophys. J. , 980, 216

Evans N. J., Kim J.-G., Ostriker E. C., 2022, Astrophys. J. Lett. , 929, L18

Giannetti A., et al., 2017, Astron. Astrophys. , 606, L12

Kennicutt Jr. R. C., 1998, Ann. Rev. Astron. Astrophys. , 36, 189

Kennicutt R. C., Evans N. J., 2012, Ann. Rev. Astron. Astrophys. , 50, 531

Kim J.-G., Ostriker E. C., Filippova N., 2021, Astrophys. J. , 911, 128

Li Y., Calzetti D., Kennicutt R. C., Hong S., Engelbracht C. W., Dale D. A., Moustakas J., 2010, Astrophys. J. , 725, 677

Licquia T. C., Newman J. A., 2015, Astrophys. J. , 806, 96

Miville-Deschênes M.-A., Murray N., Lee E. J., 2017, Astrophys. J. , 834, 57

Molinari S., et al., 2010, Publ. Astron. Soc. Pac. , 122, 314

Molinari S., et al., 2016, Astron. Astrophys. , 591, A149

Muñoz-Mateos J. C., et al., 2009, Astrophys. J. , 701, 1965

Murphy E. J., et al., 2011, Astrophys. J. , 737, 67

Murray N., Rahman M., 2010, Astrophys. J. , 709, 424

Robitaille T. P., Whitney B. A., 2010, Astrophys. J. Lett. , 710, L11

Russeil D., Zavagno A., Mège P., Poulin Y., Molinari S., Cambresy L., 2017, Astron. Astrophys. , 601, L5

Salim S., et al., 2007, Astrophys. J. Suppl. Ser. , 173, 267

Appendices

Appendix A Asymmetry parameter in a purely axisymmetric disk

In a purely circular, axisymmetric disk where the star formation rate surface density depends strictly on the Galactocentric radius $R_{\rm Gal}$ (e.g., following the exponential decay $\Sigma_{\rm SFR}(R_{\rm Gal}) \propto \exp(-R_{\rm Gal}/R_d)$ Elia et al., 2022, 2025), the Galactocentric radius at heliocentric distance D along a given line of sight is:

$$R_{\rm Gal}(D, \ell) = \sqrt{R_0^2 + D^2 - 2R_0\, D\, \cos\ell}\,. \tag{5}$$

Because $\cos(360^\circ - \ell) = \cos\ell$, lines of sight symmetrical with respect to the Sun–Galactic Center axis probe identical Galactocentric radii at each distance D. Consequently, the integrated line-of-sight SFRs are identical by symmetry, yielding $B(\ell) \equiv 0\ \forall \ell$.